Electronic Supplementary Material (ESI) for Journal of Materials Chemistry A.

In-situ grown MOFs and PVDF-HFP co-modified aramid gel nanofiber separator for high-safety lithium-sulfur batteries

Jianwei Liu[a], Jianan Wang[a,b,*], Lei Zhu[a,c], Xin Chen[a], Gong Yi[d], Qianyue Ma[a], Shiyi Sun[a], Ning Wang[e], Xiangming Cui[a], Qinqin Chai[f], Jiangtao Feng[a], Wei Yan[a,*]

[a] Department of Environmental Science and Engineering, State Key Laboratory of Multiphase Flow in Power Engineering, Xi'an Jiaotong University, 28 Xianning West Road, Xi'an 710049, China

[b] Department of Chemical and Process Engineering, Faculty of Engineering and Physical Sciences, University of Surrey, Guildford GU2 7XH, Surrey, England

[c] School of Physics and Electrical Engineering, Weinan Normal University, Chaoyang Street, Weinan 714099, China

[d] Advanced Technology Institute, University of Surrey, Guildford, Surrey GU2 7XH, England

[e] Environmental and Chemical Engineering, Xi'an Polytechnic University, Xi'an, 710048, China

[f] Xi'an Hantang Analysis & Test Co., Ltd., Xi'an, 710201, China [1]

*** Corresponding author.**

E-mail address: wangjn116@xjtu.edu.cn (Jianan Wang);

yanwei@xjtu.edu.cn (Wei Yan).

Table of Contents

Supplementary Experimental Section

1.1. Preparation of the P-PMIA separator

The P-PMIA separator was fabricated by the electrospinning method. First, PVDF-HFP (Macklin, average M_w=400000, 0.48 g) was dissolved in dimethylacetamide (DMAc, Sinopharm, 99.8%, 3 g) to obtain PVDF-HFP/DMAc solutions under 60 ℃ conditions for 1 h with vigorous stirring. Then, the corresponding PMIA (Yantai Taihe New Materials, 20 wt.%, 4.8 g) was added to the PVDF-HFP/DMAc solutions under 3 h stirring to prepare a uniform precursor. Then, a feeding rate of 0.5 mL h^{-1}, voltage of 12 kV and tip-collector distance of 13 cm were set for electrospinning. The asprepared separators were then dried at 60 °C for 2 h under vacuum conditions. The P-PMIA nanofibrous separators were obtained.

1.2. Preparation of the P-PMIA@ZIF-8 gel separator

A schematic illustration of the fabrication of the P-PMIA@ZIF-8 separator is shown in Fig. S1. The obtained P-PMIA separator was added to a mixture of 40 mL methanol (CH_3OH, Sinopharm, analytical grade), 0.5 g $Zn(NO_3)_2 \cdot 6H_2O$ and 1.2 g MIM (Sinopharm, analytical grade) and further stirred for 1 h. The P-PMIA@ZIF-8 separator was obtained after washing and drying. Finally, the gel P-PMIA@ZIF-8 separator can be obtained through hot pressure and electrolyte immersion techniques.

1.3. Characterization.

A scanning electron microscope (SEM; GeminiSEM 500, China) was used to determine the surface morphology. PANalytical X'pert MPDPro (Netherlands) X-ray diffraction (XRD) with nickel-filtered Cu Kα radiation (40 kV, 40 mA) was used to determine the sample crystallinity. A Bruker Tensor 37 spectrophotometer was used to evaluate the Fourier transform infrared (FTIR) spectra in the region between 400 and 4000 cm^{-1}. The specific surface area were conducted using Brunauer-Emmett-Teller (BET) method, and the pore diameter distribution were analyzed by both the Barrett-JoynerHalenda (BJH) and Horvath-Kavazoe (HK) methods based on N_2 adsorption-desorption tests (SSA-4300, JW-BK200B, China). The composition ratios of the separators were determined by thermogravimetric analysis (TGA) (TG-DTG-60FTIR, China). The ultraviolet–visible (UV–vis) diffuse

reflectance spectra were examined by a PE Lambda950 (China) UV-near-infrared spectrophotometer in the wavelength range of 300-900 nm. X-ray photoelectron spectroscopy (XPS) was measured by a Krators Axis ULtrabld instrument (England) with monochromatic Al Ka radiation (1486.6 eV) radiation. The liquid electrolyte wettability was estimated by a DSA100 (Germany) contact angle meter. An ICP-AES-9000 inductively coupled plasma-atomic emission spectrometry instrument (Japan) was used to determine the S content of the lithium metal anodes. The mechanical properties of separators were tested by an Instron 5548 (America) microtester machine. The tensile strength were measured at a stretching speed of 5 mm min^{-1} with the sample straps of about 20 mm wide and 40 mm long. The unit X (cN) of the tested values can be converted to Y (MPa) in accordance with equation (1).

$$Y = \frac{X}{A \times d} \tag{1}$$

where A was the width (cm) and d was the separator thickness (μm).

The puncture strength were tested on a lab-made sample holder with a gap width of 1cm was used to fix the tested separators, and the rate of compression displacement was set to be 1 mm min^{-1}. the Young's modulus of separators via using atomic force microscope (AFM, SPM-9700HT, Japan)

The liquid electrolyte retention capacity (ε) of the separators was computed using equation (1):

$$\varepsilon = \frac{M_b - M_a}{M_a} \times 100\% \tag{2}$$

where M_a and M_b are the mass separators of the initial and after immersion in liquid electrolyte for 24 hours, respectively, mg.

1.4. Li-S battery assembly and electrochemical measurements

Electrochemical tests were conducted by assembling 2032 coin-type half-cells in an argon-filled glove box where the oxygen and water contents were below 0.1 ppm (DELLIX LS750S). The sulfur cathode materials (CNT/S) were mixed sulfur with sulfur (280 mg), CNT (80 mg) and PVDF (40 mg) in a weight ratio of 7:2:1 in NMP (1.8 mL) and stirred to obtain a uniform slurry, which was then coated on aluminum foil/CNF, vacuum-dried at 60 °C

overnight and used to form the sulfur electrodes.The S content is 70 % and the mass loading of sulfur is ~1.5 mg cm^{-2}. Li metal (Tianjin Zhongneng) and Celgard 2500 PP/as-prepared separators were used as the anode and separator, respectively. The electrolyte was composed of 1.0 M lithium bis (trifluoromethanesulfonyl)imide in a solvent mixture of DME/DOL (1:1 by volume) with 1.0% $LiNO_3$ additive. The quantity of electrolyte was controlled at 10-15 μL per 1 mg of sulfur (E/S=10-15). Galvanostatic charge-discharge measurements were conducted using a LANHE (China) battery tester within a voltage window of 1.7-2.8 V vs. Li/Li^+). Cyclic voltammetry (CV) was obtained on an electrochemical workstation (CHI 660D, China). Electrochemical impedance spectra (EIS) were measured with a 0.01- 100 kHz frequency range

The lithium diffusion process can be demonstrated according the Randles-Sevcik equation (2)

$$I_p = 2.69 \times 10^5 n^{1.5} A D_{Li^+}{}^{0.5} C_{Li^+} v^{0.5} \quad (3)$$

where *Ip* is the peak current. n is the electron transfer (2). A is the electrode area (cm^2). D_{Li+} is the ithium-ion diffusion rate (cm^2 S^{-1}). v is the scan rate (V s^{-1}). C_{Li+} is the Li^+ concentration of the electrolyte (mol mL^{-1})

The ionic conductivities (σ) of the separators at room temperature were measured on symmetric cells with two stainless steel electrodes with an alternating-current (AC) amplitude of 1 mV over the frequency range from 0.1 to 10^5 Hz. The bulk resistance of a separator (R_0) was determined by the intercept of the Nyquist plot with the real axis. The ionic conductivity was then calculated from:

$$\sigma = \frac{d}{R_0 S} \quad (4)$$

where d (μm) is the thickness and S (cm^2) is the contact area of the separator and the electrode.

The electrochemical stability windows of various separators were measured through LSV by Li || separator || SS batteries at a scan rate of 5 mV s^{-1} from 1.8-6 V.

The Li^+ transference number (t_{Li+}) of the separators was obtained by the Li || separator || Li batteries via EIS and DC potentiostatic polarization measurements, and t_{Li+} was calculated according to the Bruce-Vincent-Evans equation:

$$t_{Li+} = \frac{I_S(\Delta V - I_O R_o)}{I_O(\Delta V - I_S R_s)} \quad (5)$$

where ΔV is the applied DC polarization voltage (0.01 V), R_o and R_s represent the interfacial resistances before and after polarization, respectively, and I_o and I_s are the initial currents before the DC polarization and the stable current after the DC polarization.

1.5. Computational methods

Adsorption energies were calculated using Gaussian 09 software, which employs the density functional theory (DFT) method. To have a better discussion on the affinity of CMPA towards differing microscale LiPSs, the interactions of CMPA with a series of Lithium-polysulfides radicals at a molecular level were calculated. The geometries of the molecular were optimized through B3LYP/6-31+ basis set, followed by the adsorption energy calculation.

The adsorption energies of Li_2S_x ($2 \leq x \leq 8$) were defined as follow:

$$\Delta E_{ads} = E_{CMPA+Li_2S_x} - E_{CMPA} - E_{Li_2S_x}$$

where $E_{CMPA+Li2Sx}$ is the electronic energy of the CMPA molecular with sulfur species which adsorbed on the CMPA molecular, E_{CMPA} is the electronic energy of the CMPA molecular, and E_{Li2Sx} is the electronic energy of Li_2S_x molecules. Based on this definition, a more negative value indicates a stronger binding system.

1.6. Preparation of Li_2S_6 solution

0.005 M Li_2S_6 (30 mM in sulfur) was prepared by chemically reacting sulfur with Li_2S in 1,3-dioxolane/1,2dimethoxyethane solution (DOL/DME, 1:1 by volume).

Supplementary Figures

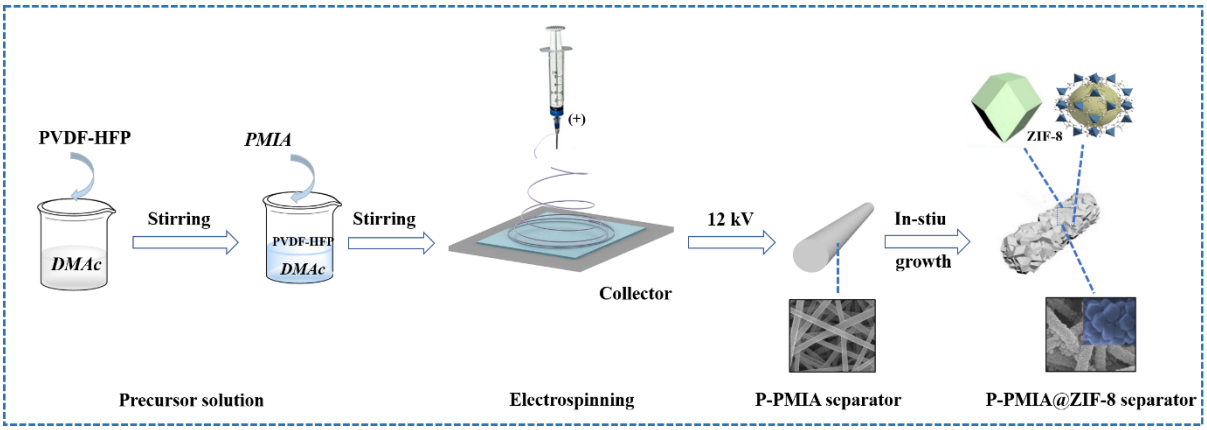

Fig. S1. Schematic illustration of the fabrication of the P-PMIA@ZIF-8 separator

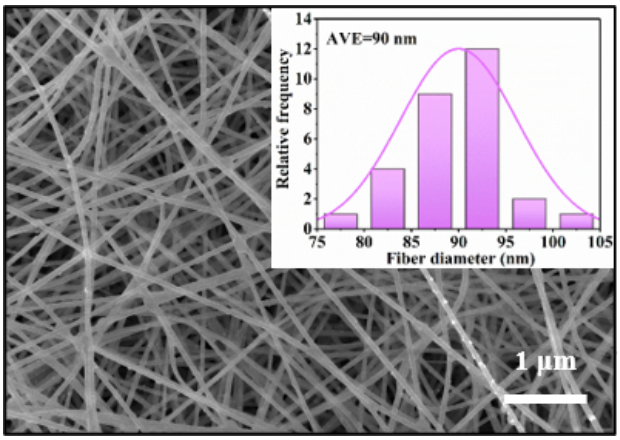

Fig. S2. SEM image of the PMIA separator and corresponding fiber diameter distribution.

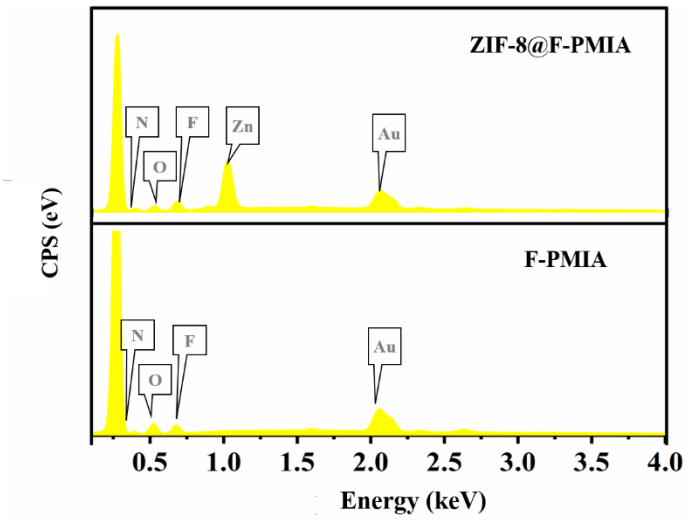

Fig. S3. EDS images of the P-PMIA and P-PMIA@ZIF-8 separators

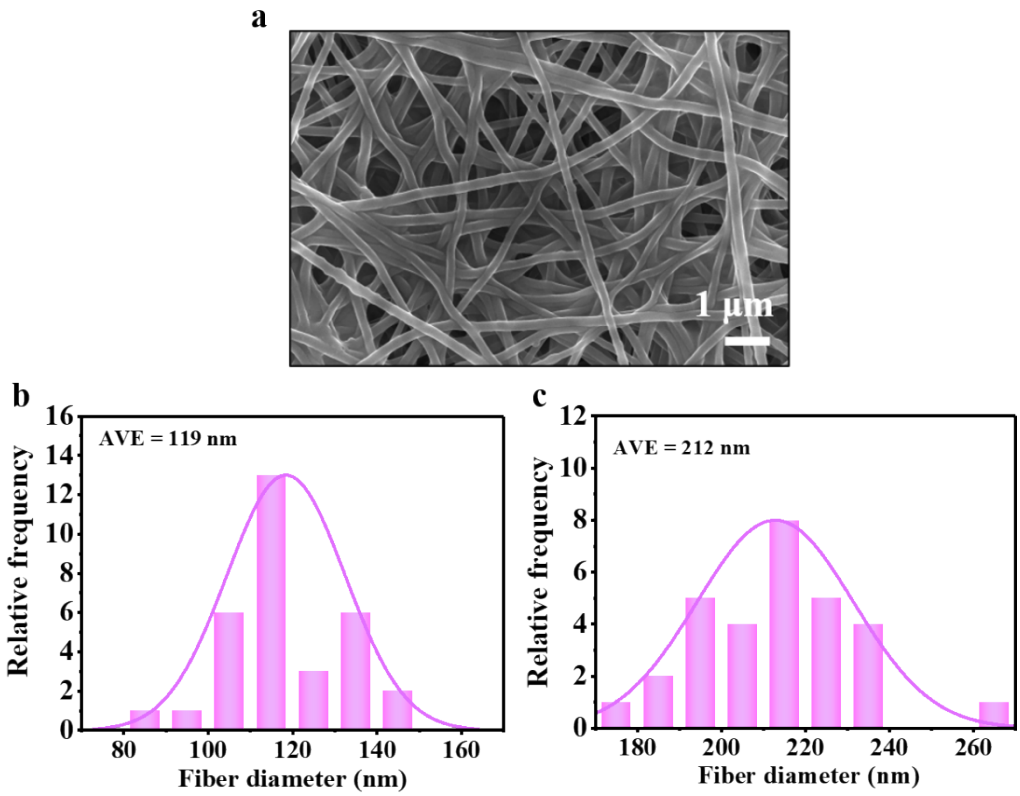

Fig. S4. a) SEM images of PMIA separator and the average diameter of b) P-PMIA and c) P-PMIA@ZIF-8 nanofibers after the immersion of liquid electrolyte.

The formation mechanism of the gelation state could be explained by the following reasons. Firstly, the "incursion" of electrolyte appeared from the outside to the pores of polymeric substance, and then the continuous solution penetrates into the holes in the polymer chains to form a swollen polymer network[2]. Secondly, The C-F bonds in P-PMIA separator (Fig. 2b and e) exhibit high polarity and low surface energy, which can achieve conspicuous complexation with the lithium salts[3]. In addition, the interaction between the fluorinated polymer and lithium salts in the electrolyte can be strengthened due to the Lewis acid-base effect and the reduced crystallinity resulting from the addition of the prepared MOFs nanoparticles.

The diameters of both P-PMIA and P-PMIA@ZIF-8 nanofibers increased after soaking by electrolyte. The average diameter of P-PMIA nanofibers increased from 81nm (Fig. 1a) to 119 nm with an obvious swelling behavior. As comparison, the P-PMIA@ZIF-8 nanofibers show a weaker swelling phenomenon with the fiber diameter increasing from 189 nm (Fig. 1b) to 212 nm. The phenomenon can be explained by the following reasons. As the loading of ZIF-8 nanoparticles, the upper surface of the P-PMIA@ZIF-8 separator are mostly covered with the microporous ZIF-8 nanoparticles. Hence, the solution will not continue to be supplied into the

pores from outside even if the polymer chain network has not reached swelling saturation[2]. Meanwhile, the high strength of the ZIF-8 nanoparticles interlinked on the surface can also offset the swelling of the polymer fibers[4, 5].

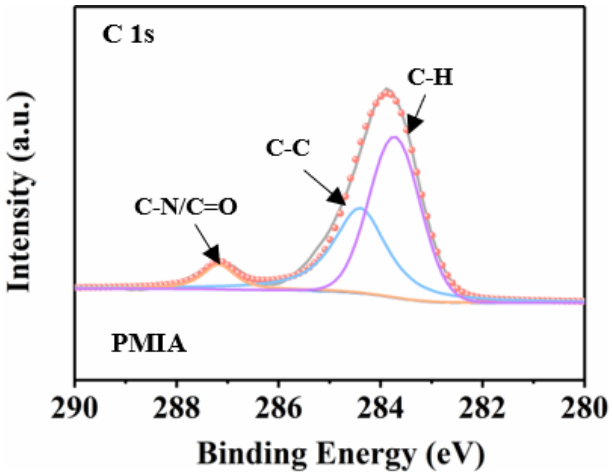

Fig. S5. XPS spectrum of PMIA separator after the immersion of liquid electrolyte.

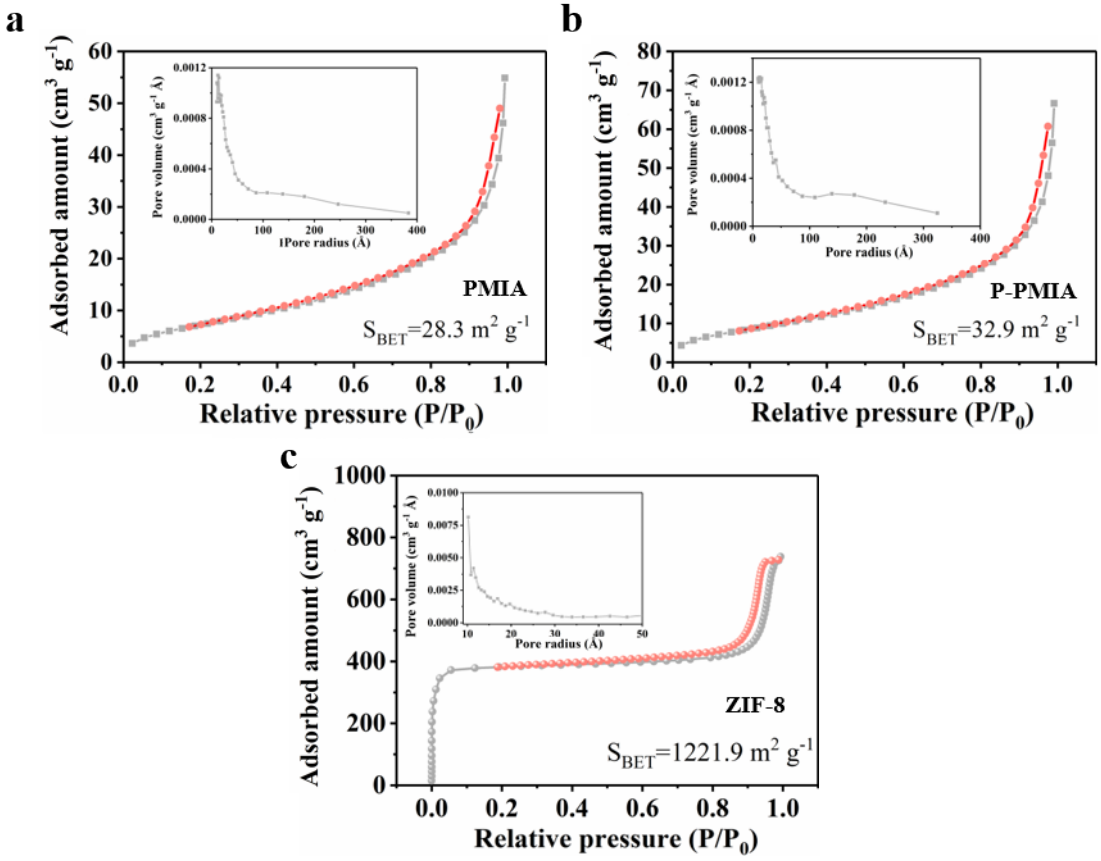

Fig. S6. N_2 adsorption-desorption curves and pore distributions of a) PMIA, b) P-PMIA and c) ZIF-8.

Additionally, the nitrogen sorption isotherm for ZIF-8 observes the type I isotherm, indicating the existence of micropore structure[1].

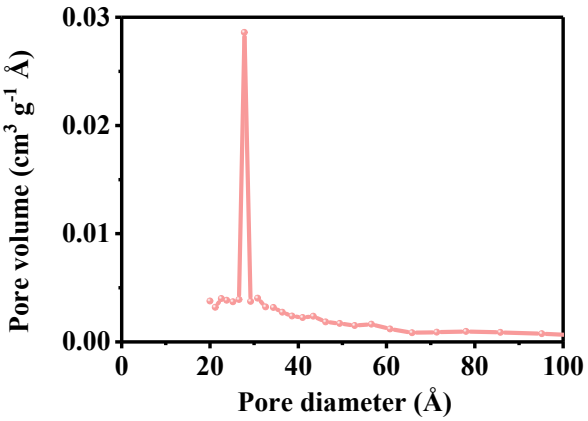

Figure S7. The enlarged Figure 3a on the pore distribution for P-PMIA@ZIF-8 separator

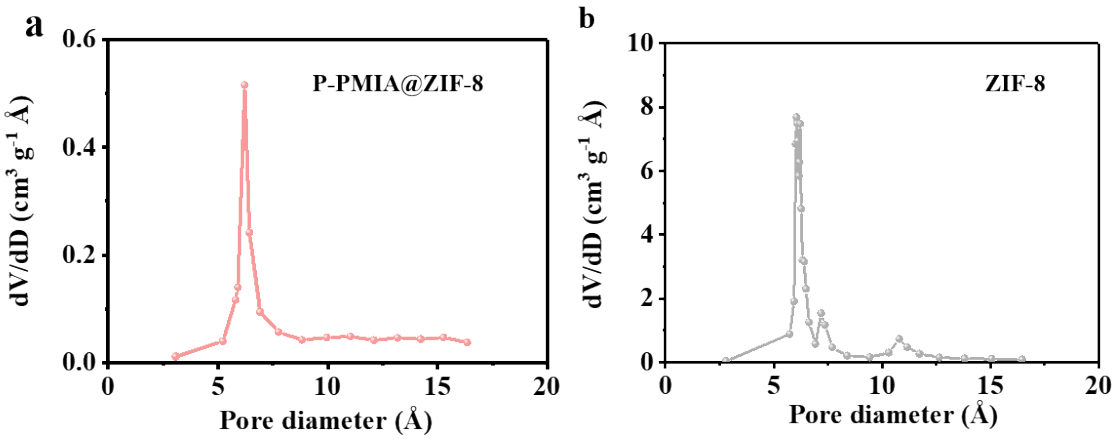

Fig.S8 The microporous size distribution of P-PMIA@ZIF-8 separator and ZIF-8 nanoparticles.

Fig. S8 shows that the main diameter distribution of the microporous ZIF-8 nanoparticles concentrates on about 6.0~6.2 Å, which is almost consistent with that of the P-PMIA@ZIF-8 separator (~6.2 Å). This result indicates the inherent microporous structure of ZIF-8 nanoparticles could be well inherited after they were in-situ introduced onto the P-PMIA nanofibers.

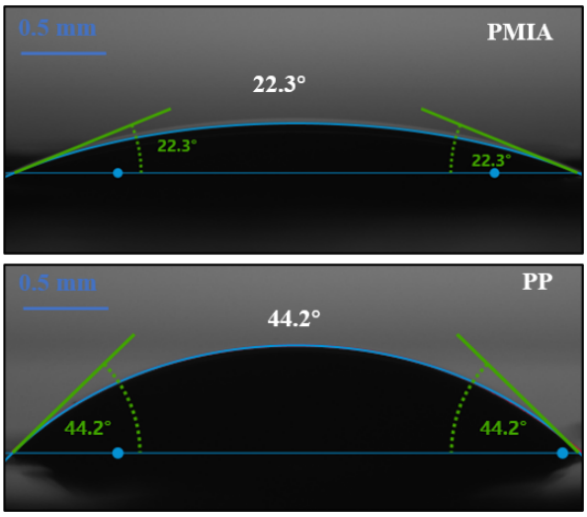

Fig. S9. Contact angle images of the PP and PMIA separators.

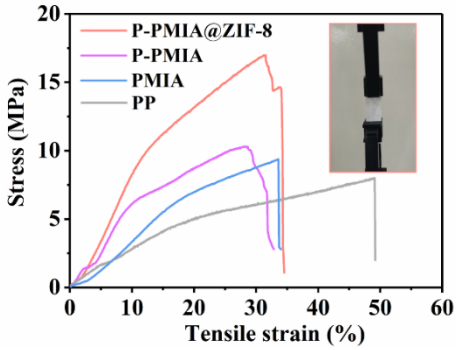

Fig. S10. The puncture strength curves the PP, PMIA, P-PMIA and P-PMIA@ZIF-8 separators.

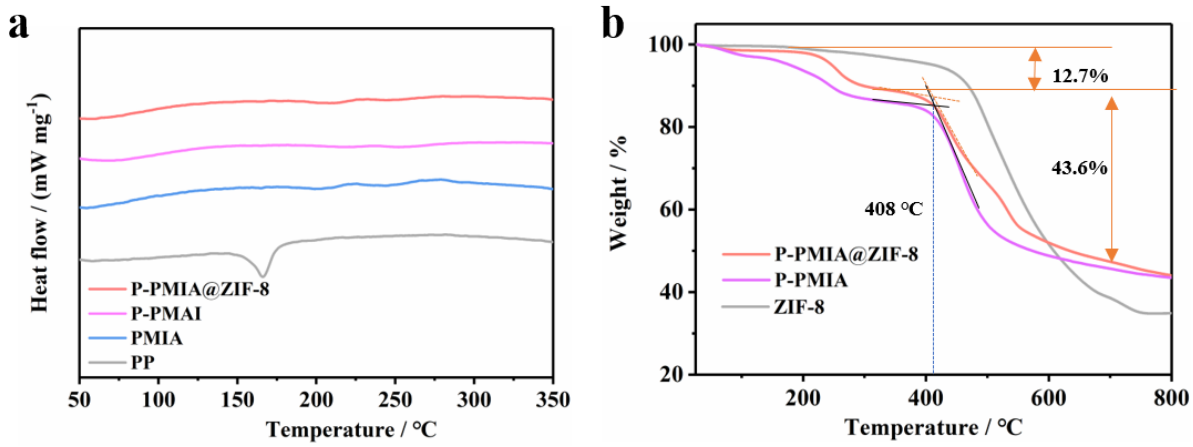

Fig. S11. a) DSC curves of PP separator and various PMIA-based separators. b) TG curves of ZIF-8, P-PMIA and P-PMIA@ZIF-8.

From Fig. S8a, an evident endothermic peak at around 170.1 °C appeared in the DSC curve of the commercial PP separator, corresponding to the typical melting temperature of PP[6]. By comparison, the corresponding curves of various PMIA samples were similar to straight lines without any endothermic peaks, revealing their high thermal stability up to 250 °C. The TG results are shown in Fig. S8b. The initial weight loss below 100 °C for the nanofiber membrane was due to the loss of moisture and residual solvents. The major weight loss at 400-800 °C was due to the rupture of intraand intermolecular hydrogen bonds and the breakdown of the aramid bond of PMIA molecular chains[7].

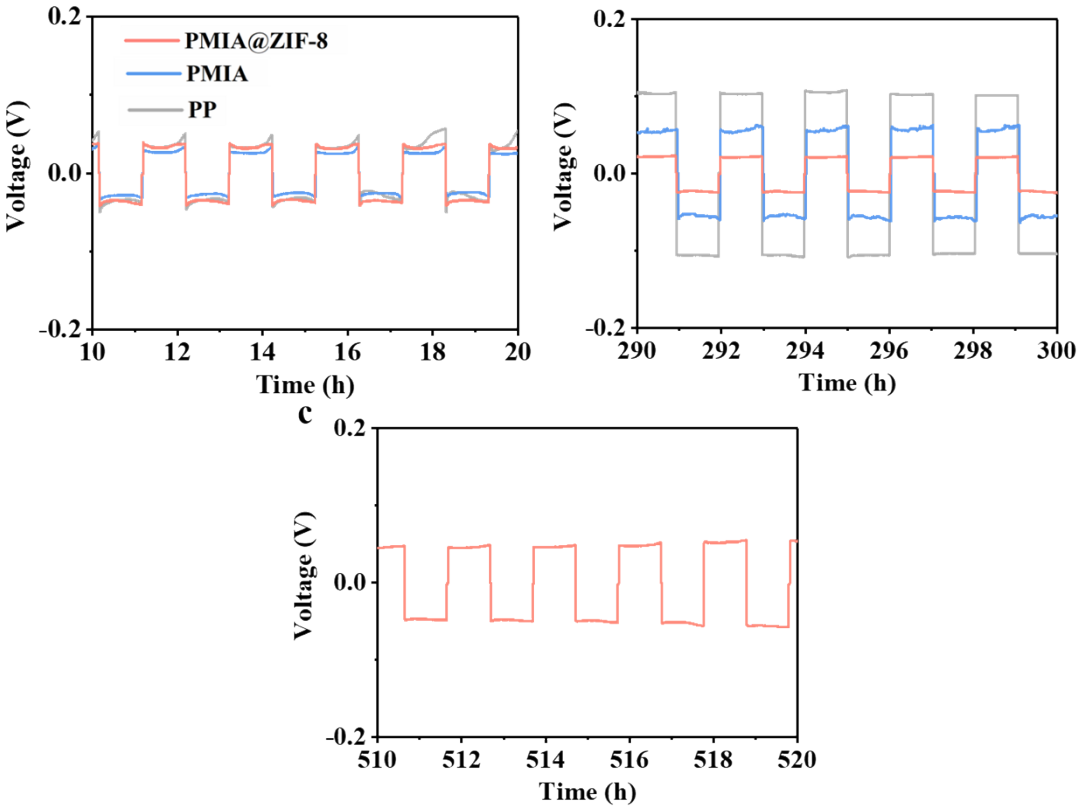

Fig. S12. The partial voltage profiles for Li||Li symmetric cells with PP, P-PMIA and P-PMIA@ZIF-8 separators at a current density of 1 mA cm^{-2} with an areal capacity of 1 mAh cm^{-2}

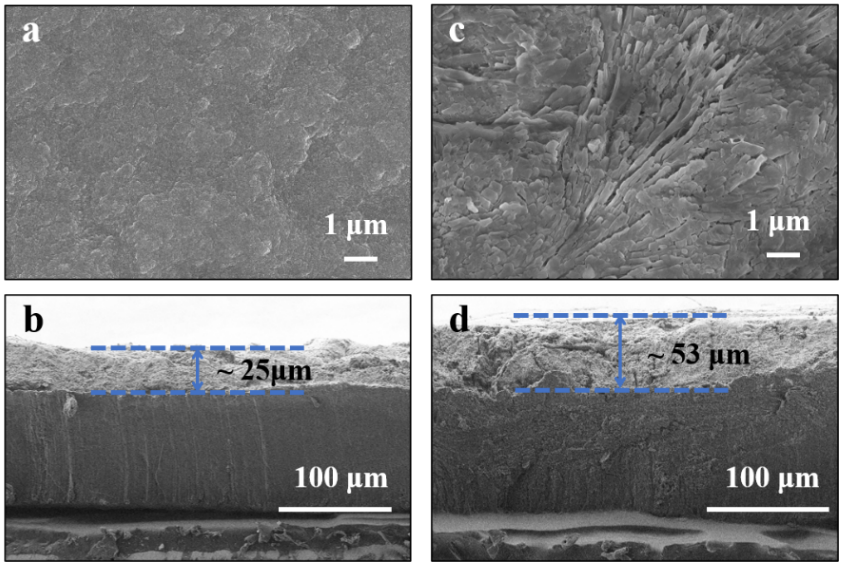

Fig. S13.The top view and cross-sectional SEM images of the lithium anodes with a-b) PP separator and c-d) P-PMIA@ZIF-8 separator after 100 h at a current density of 1 mA cm^{-2} with an areal capacity of 1mAh cm^{-2}.

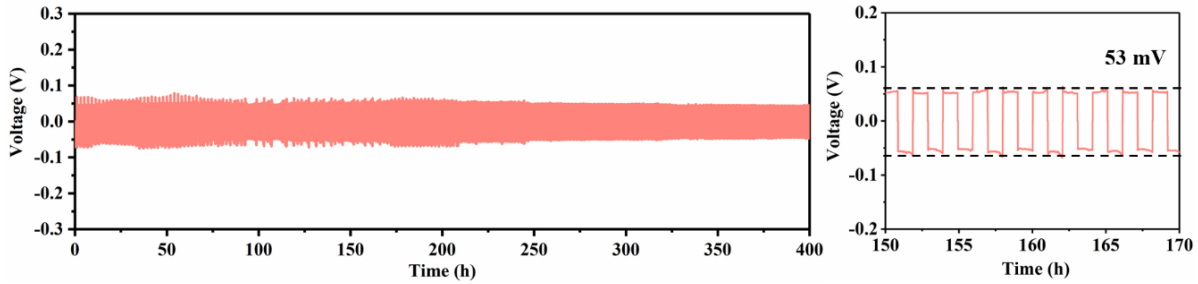

Fig. S14. The voltage profiles in Li||Li symmetric cells with a P-PMIA@ZIF-8 separator at 3 mA cm^{-2} with a stripping/plating capacity of 3 mAh cm^{-2}

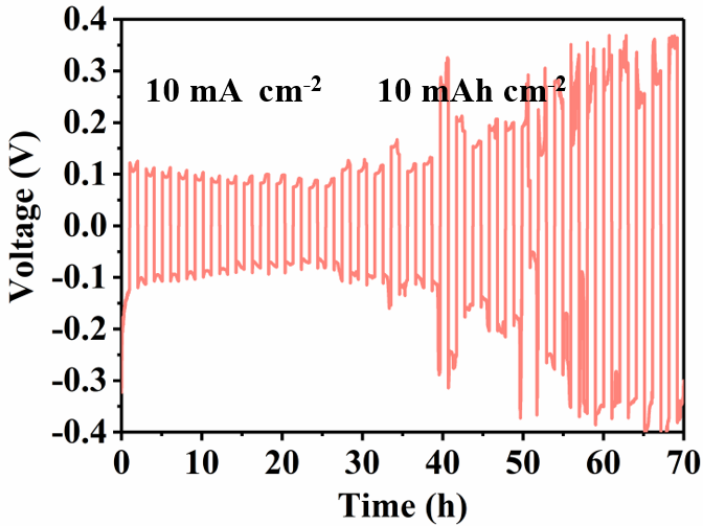

Fig. S15. The voltage profiles in Li||Li symmetric cells with a P-PMIA@ZIF-8 separator at 10 mA cm^{-2} with a stripping/plating capacity of 10 mAh cm^{-2}.

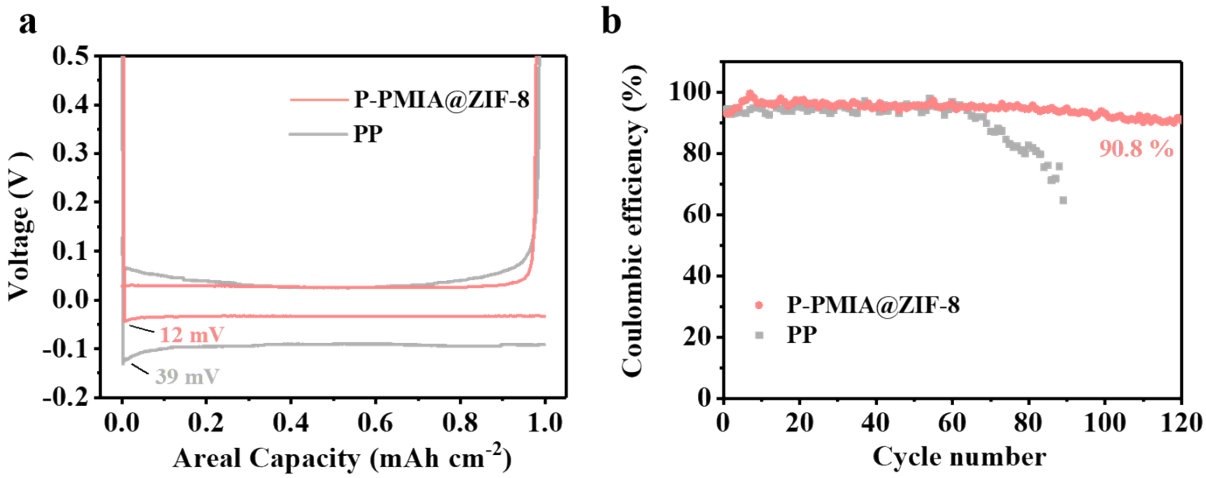

Fig. S16. a) The voltage profiles of Li plating/stripping and b) Cycling CEs for Li||Cu batteries with PP and P-PMIA@ZIF-8 separator at 1 mA cm^{-2} and 1 mAh cm^{-2}.

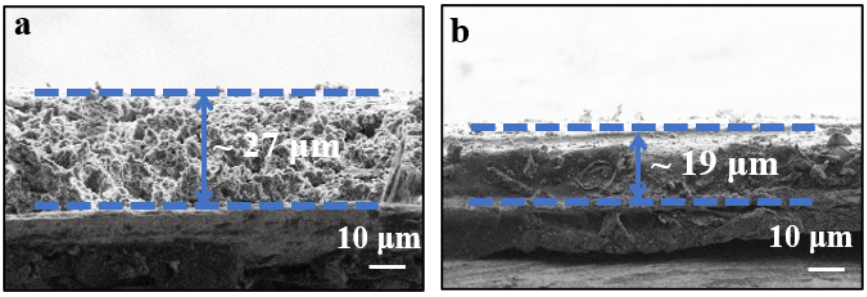

Fig. S17 The cross-sectional images of the deposited Li on Cu foil with a) PP separator b) P-PMIA@ZIF-8 separator after cycling at 1 mA cm^{-2} and 1 mAh cm^{-2}.

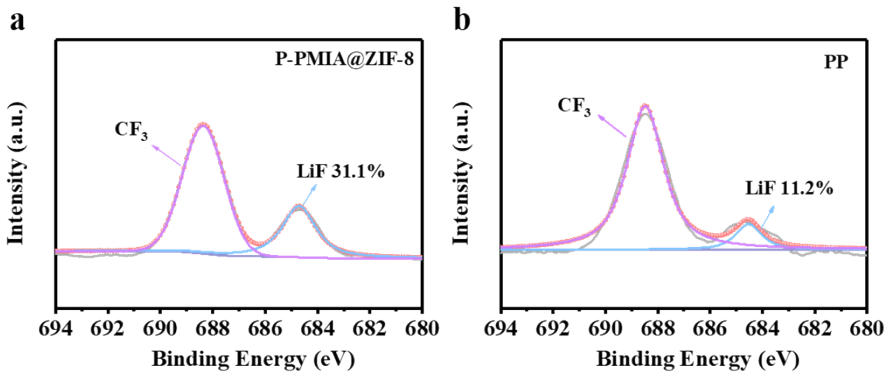

Fig. S18 The F 1s XPS spectra of the Li anodes with P-PMIA@ZIF-8 and PP separators after 30 cycles

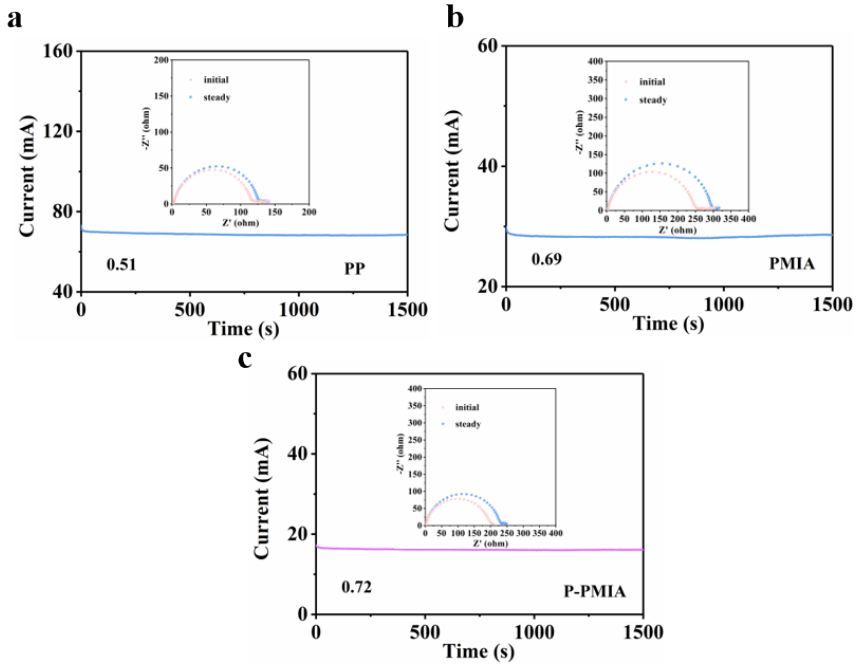

Fig. S19. a) Li||PP||Li, b) Li||PMIA||Li and c) Li||P-PMIA||Li symmetric cells, before and after polarization; inset: variation of current with time during polarization at an applied voltage of 10 mV.

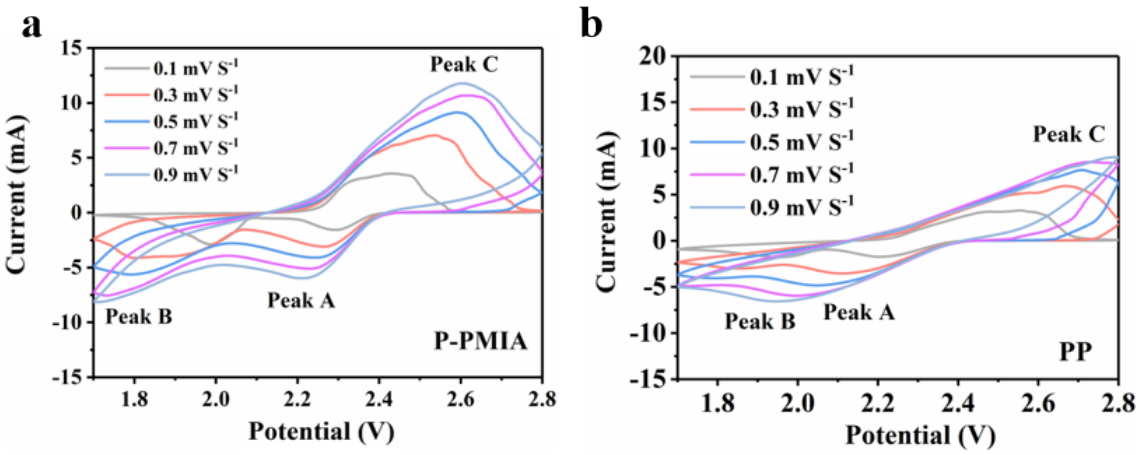

Fig. S20. Plots of CV peak current for the a) first cathodic reduction process (peak A: $S_8 \rightarrow Li_2S_x$), b) second cathodic reduction process (peak B: $Li_2S_x \rightarrow Li_2S_2/Li_2S$) and (c) anodic oxidation process (peak C: $Li_2S_2/Li_2S \rightarrow S_8$) versus the square root of the scan rates.

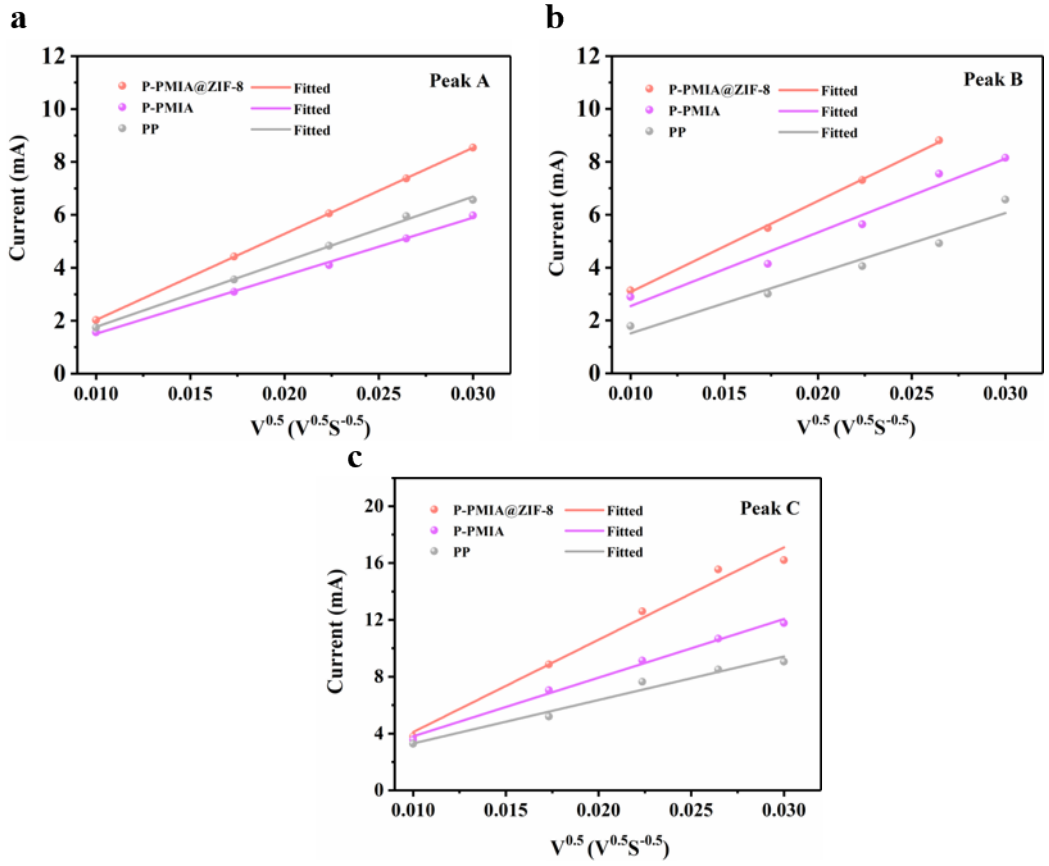

Fig. S21. Plots of CV peak current for the a) first cathodic reduction process (peak A: $S_8 \rightarrow Li_2S_x$), b) second cathodic reduction process (peak B: $Li_2S_x \rightarrow Li_2S_2/Li_2S$) and c) anodic oxidation process (peak C: $Li_2S_2/Li_2S \rightarrow S_8$) versus the square root of the scan rates.

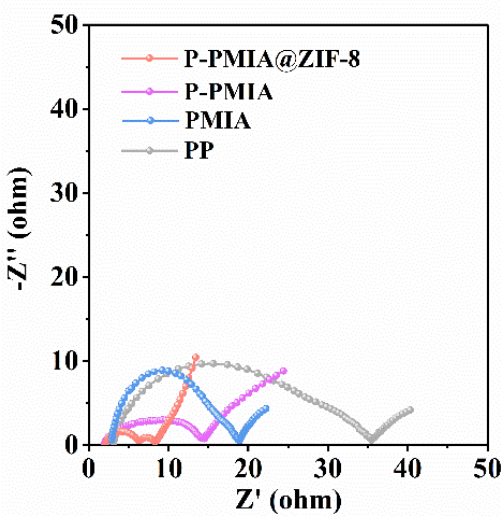

Fig. S22. Nyquist plots of PP and various PMIA-based separators after 200 cycles

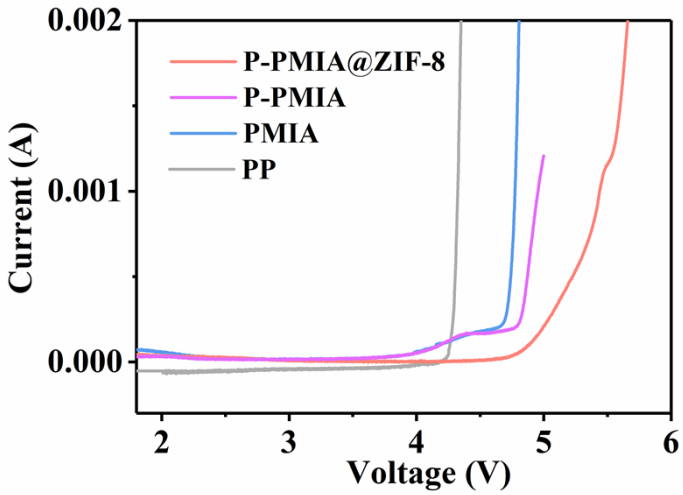

Fig. S23. Electrochemical window plots of PP, PMIA, P-PMIA and P-PMIA@ZIF-8 separators.

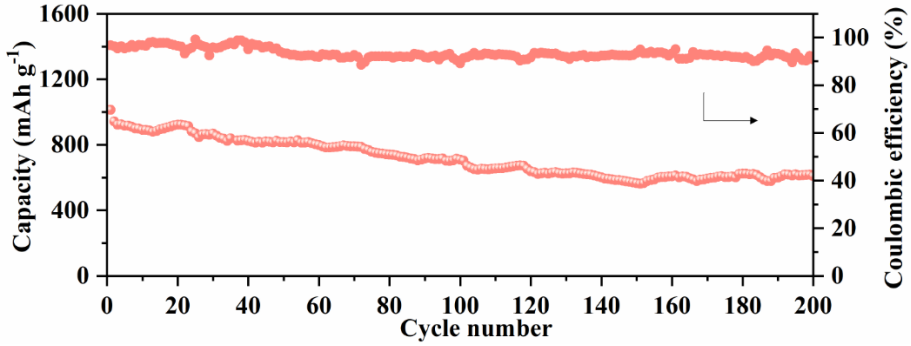

Fig. S24. Long-term cycling performance of the P-PMIA separator at an enhanced densities of 1 C for 200 cycles.

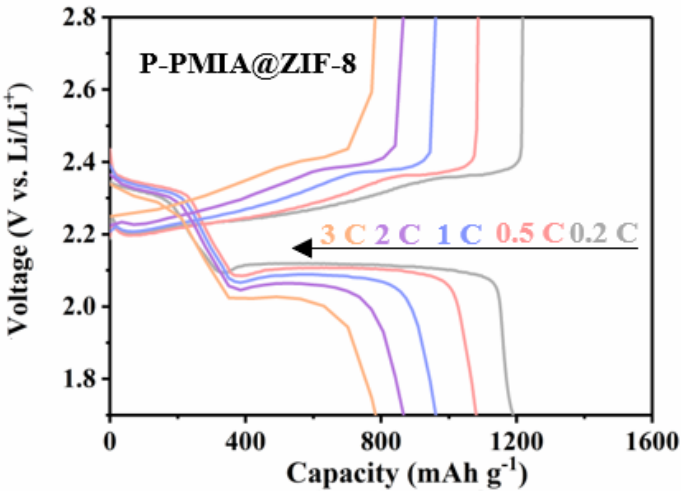

Fig. S25. Galvanostatic charge/discharge profiles from 0.2 to 3 C.

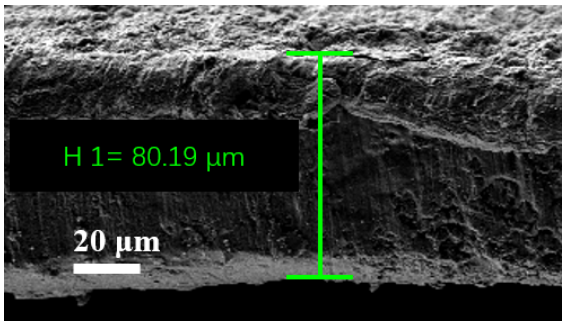

Fig. S26. Cross-sectional SEM image of the thinner Li anodes.

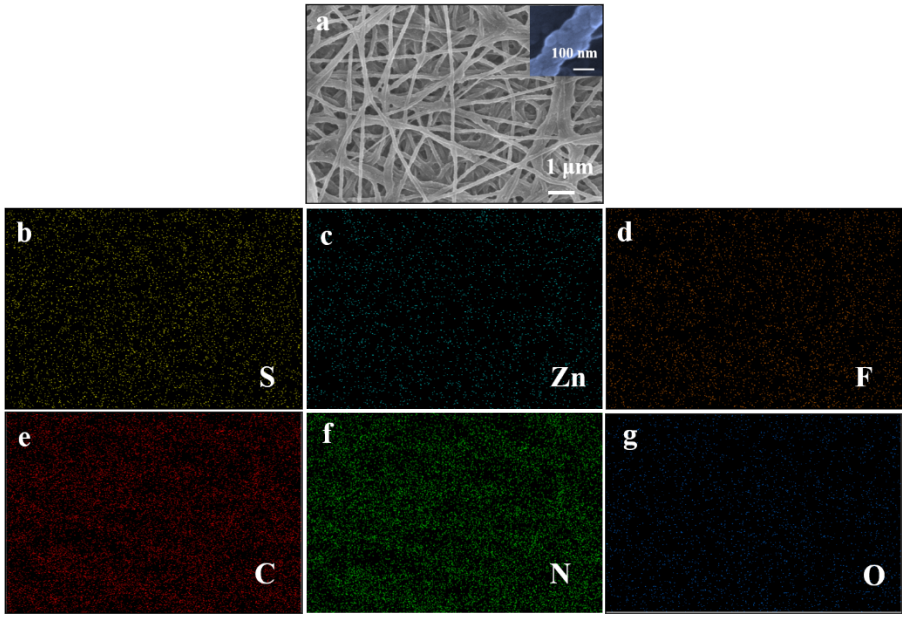

Fig. S27. a) SEM and b-g) EDS mapping images of the P-PMIA@ZIF-8 separator (toward cathode side) after 300 cycles in Li-S coin cells.

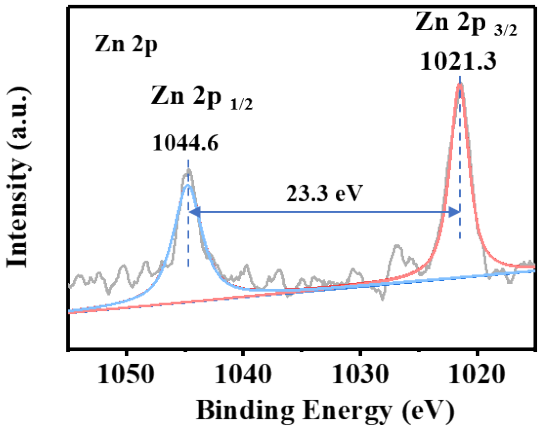

Fig. S28 The Zn 2p XPS spectra of the P-PMIA@ZIF-8 separator after 300 cycles

Fig. 28 illustrates the Zn 2p spectra of ZIF-8 in P-PMIA@ZIF-8 separator after 300 cycles. The binding energies of 1021.3 eV and 1044.6 eV for Zn 2p in the spectrum can be attributed to Zn 2p3/2 and Zn 2p1/2, respectively. The differernce binding energy of 23.3 eV confirms the unchanged valence state of Zn^{2+} in P-PMIA@ZIF-8 separator and the high stablity of ZIF-8 nanoparticles during cycling[8].

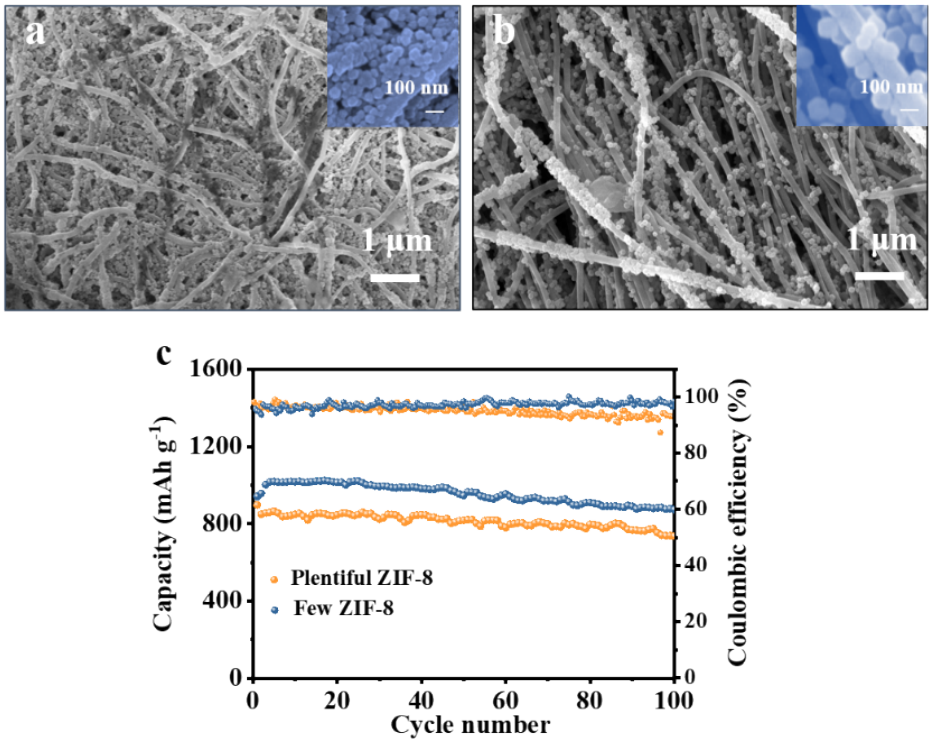

Fig. S29 The SEM image of a) excessive ZIF-8 modified composite separator and b) just a few ZIF-8 modified composite separator. c) Cycling performance of separators at 0.2 C with plentiful ZIF-8 and few ZIF-8 modified composite separator

The excessive ZIF-8 nanoparticles are prone to cause the unfavorable agglomeration and hence hinder the lithium-ion diffusion/flow. As comparison, just a few ZIF-8 nanoparticles on P-PMIA separator can also hardly resist the Li_2S_x diffusion because of the large microporous gaps among particles and the low surface area. As a result, the batteries with excessive ZIF-8 and just a few ZIF-8 modified composite separator retain 739 mAh g^{-1} and 880 mAh g^{-1} after 100 cycles at 0.2 C, respectively, much lower than that of the normal P-PMIA@ZIF-8 separator (990 mAh g^{-1}) (Fig. 5f)

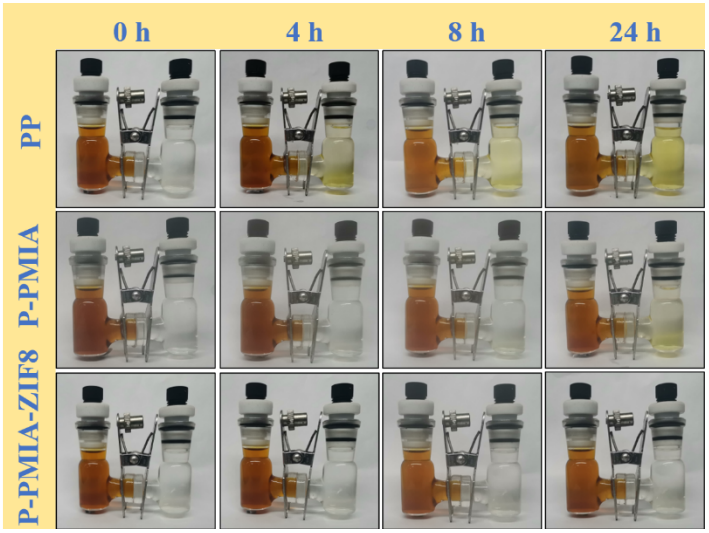

Fig. S30. Li_2S_x diffusion tests for the PP, P-PMIA and P-PMIA@ZIF-8 separators.

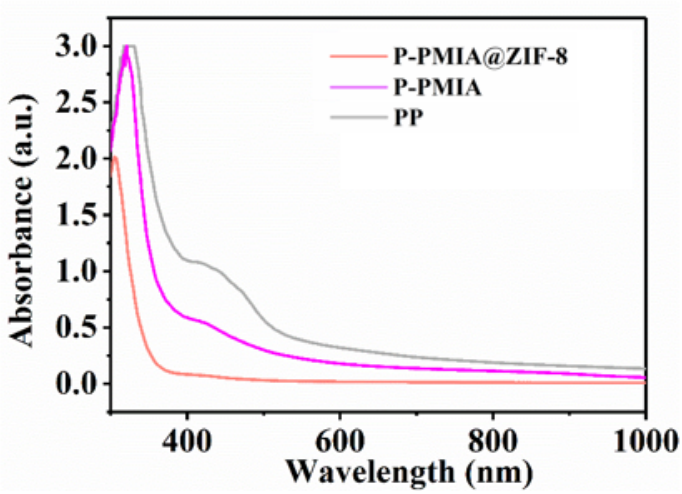

Fig. S31. UV-vis spectra of the Li_2S_6 solution with PP, P-PMIA and P-PMIA@ZIF-8 separators.

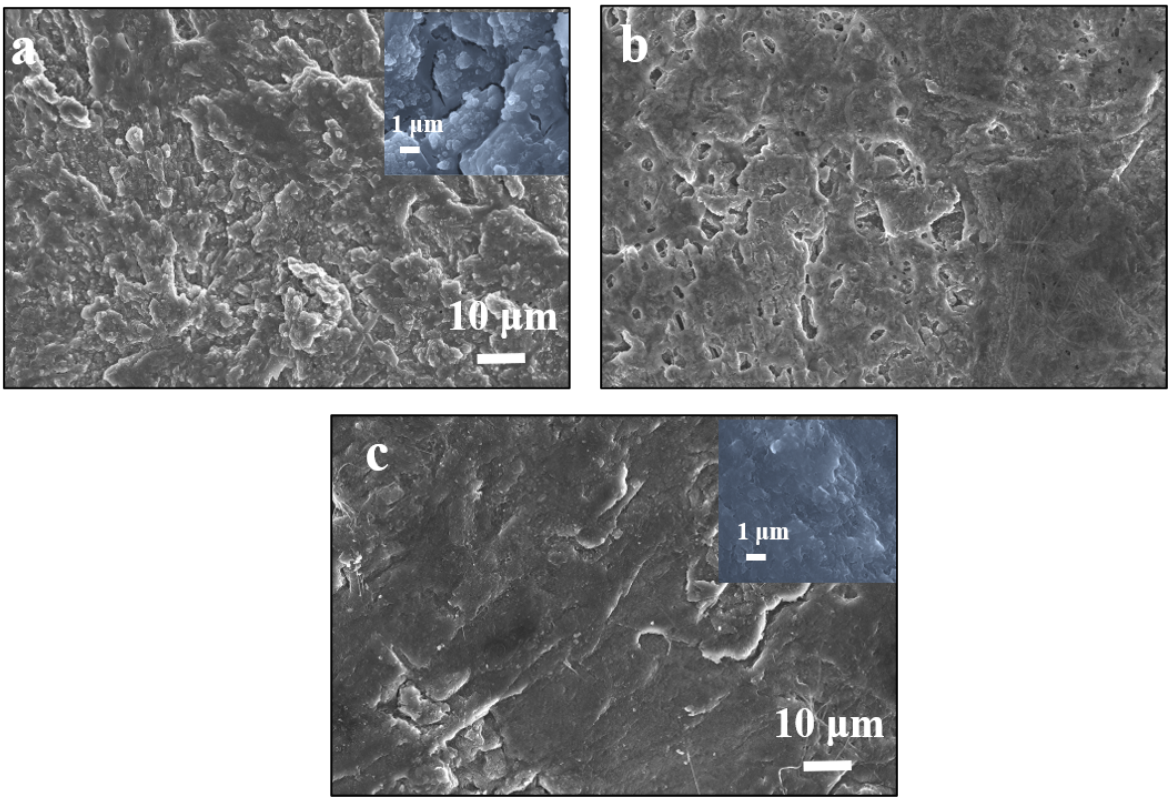

Fig. S32. The surface morphologies of the lithium-metal anode disassembled from Li-S batteries after 150 cycles using a) PP, b) P-PMIA and c) P-PMIA@ZIF-8 separators.

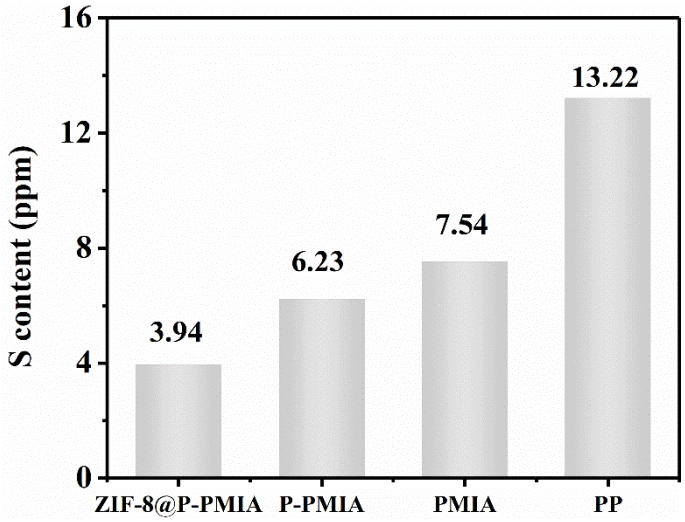

Fig. S33. S content of the lithium metal anodes probed by ICP-AES for the various separators after 150 cycles.

Supplementary Tables

Table S1. Thickness (d), bulk resistance (R_0), and ionic conductivity (σ) of various separators

Samples	d (μm)	R_0 (Ω)	σ (10^{-3} S cm^{-1})
PP	25	2.76	0.45
PMIA	28	1.32	1.05
P-PMIA	27	1.01	1.32
P-PMIA@ZIF-8	29	0.87	1.66

Table S2. Comparisons of the lithium-ion diffusion rate (D_{Li+}) of the various separators.

Materials	lithium-ion diffusion rate D_{Li+} (cm^2 S^{-1})		
	Peak A	Peak B	Peak C
P-PMIA@ZIF-8	7.69×10^{-8}	8.62×10^{-8}	3.08×10^{-7}
P-PMIA	3.49×10^{-8}	5.62×10^{-8}	1.22×10^{-7}
PP	4.41×10^{-8}	3.53×10^{-8}	6.56×10^{-8}

Table S3. Related resistance values obtained from the impedance spectra in Fig.4b

Battery	Re (Ω)	Rct (Ω)	Measurement errors
P-PMIA@ZIF-8	1.56	62.1	≤4.51 pct
P-PMIA	1.64	82.4	≤4.67 pct
PMIA	1.29	86.1	≤4.83 pct
PP	1.62	154.3	≤5.27 pct

Table S4. Related resistance values obtained from the impedance spectra in Fig.S14.

Battery	Re (Ω)	Rct (Ω)	Rs (Ω)	Measurement errors
PMIA@ZIF-8	2.52	1.4	3.93	≤5.54 pct
P-PMIA	1.9	12	7.8	≤5.01 pct
PMIA	1.34	18	6.6	≤5.32 pct
PP	3.0	19	12	≤2.68 pct

Table S5. Comparison of the discharge specific capacities of P-PMIA@ZIF-8 separator at various current densities with those of other reported separator materials.

Materials	Reversible capacity (mAh g^{-1})				Reference
	0.2 C	0.5 C	1 C	2 C	
Polyimide separator	815	679	590	451	[9]
PCNF@GF separator	1082	877	716	539	[10]
A PVDF-HFP based gel electrolyte	866	475	308	243	[11]
PAL separator	920	790	650	590	[12]
Co/NCNS/CNT coated separator	1142	989	910	841	[13]
UiO-66-SO_3-PVDF separator	1069	926	813	696	[14]
NSPCF@CoS_2 separator	863	776	649	489	[15]
BNNs@CNFs-rGO@Ru SAs	1080	862	692	583	[16]
P-PMIA@ZIF-8 separator	**1187**	**1080**	**961**	**867**	**This work**

Table S6. Calculations of the N/P ratio in the current Li-S coin with various separators

thickness (Li) (μm)	**Cathode (PE)**				**Anode (NE)**				**N/P ratio**
	Electrode area (cm^{-2})	Active S loading (mg cm^{-2})	Areal specific capacity (mAh cm^{-2})	Specific capacity (mAh)	Electrode area (cm^{-2})	Active material loading (mg cm^{-2})	Areal specific capacity (mAh cm^{-2})	Specific capacity (mAh)	
Conventional Li-S battery	1.54	1.5	1.26	1.94	2.01	10.68	41.22	82.85	42.7
Li-S battery (Li) 200 This work	1.54	6.93	11.61	17.88	2.01	10.68	41.22	82.85	4.6
Li-S battery (Li) 80 This work	1.54	6.45	10.80	16.63	2.01	4.27	16.48	33.12	2.0

*The defined specific capacity is 1675 mAh g^{-1} for sulfur and 3860 mAh g^{-1} for lithium. The diameters of the cathode and the anode discs in the coin batteries were fixed to be 14 and 16 mm, respectively; The density of Li anode is 0.534 g cm^{-3}.

Table S7. Calculations of the areal weight for various Li-S batteries.

Battery	Current collector (mg cm^{-2})	Active layer (mg cm^{-2})	Separator (mg cm^{-2})	Electrolyte (mg cm^{-2})	Li anode (mg cm^{-2})	Total weight (mg cm^{-2})
Conventional Li-S battery	5.35 (Al foil)	2.14 (active S) (1.5 mg cm^{-2})	1.26	25.80 (23 μL) (E/S = 15)	10.68	45.23
Li-S battery (200 μm) (In this work)	1.78 (CNFs)	9.90 (active S) (6.93 mg cm^{-2})	1.42	54.88 (49 μL) (E/S = 7)	10.68	77.25
Li-S battery (80 μm) (In this work)	1.67 (CNFs)	9.21 (active S) (6.45 mg cm^{-2})	1.44	36.12 (μL) (E/S = 5)	4.27	52.71

*The mass of electrolyte is measured to be 1.12 mg ul^{-1}; The density of Li anode is 0.534 g cm^{-3};The mass ratio of the active sulfur to the whole active layer was 70%.

The conventional Li-S batteries were commonly assembled by an Al foil current collector with low sulfur areal loading (<2.0 mg cm^{-2}), a widely used and thick commercial lithium (>400 μm) and a high E/S ratio (>15 mL g^{-1}). The area weights of various components in conventional Li-S battery were provided in Figure 6e and Table S4. In this work, to evaluate the performance of P-PMIA separator in practical Li-S batteries, the Li-S cells were assembled by a lighter CNFs current collector with high sulfur areal loading and a thinner lithium anode and a lower E/S ratio. In addition, lithium foils with different thicknesses (200 μm and even 80 μm) were tested as the anode to further control the N/P ratio of batteries, as shown in Table S4.

The cell-level gravimetric energy density values for Li-S coin battery-200 and Li-S coin battery-80 were also calculated based on the whole basic units of the battery system (neglecting the mass of any packaging material), as shown in the following formula.

$$\frac{\text{Capacity mAh g}^{-1} \times 2.15\ \text{V} \times \text{mass (S) mg cm}^{-2}}{\left(m_{\text{Current collector}} + m_{\text{Active layer}} + m_{\text{Electrolyte}} + m_{\text{Separator}} + m_{\text{Li}}\right) \text{mg cm}^{-2}}$$

The cell-level gravimetric energy density value for conventional Li-S coin battery-200:

$839 \times 2.15 \times 1.5/45.23 = 60\ \text{Wh} \cdot \text{kg}_{\text{cell}}^{-1}$

The cell-level gravimetric energy density value (1st cycle) for Li-S coin battery-200:

$880 \times 2.15 \times 6.93/77.25 = 169\ \text{Wh} \cdot \text{kg}_{\text{cell}}^{-1}$

The cell-level gravimetric energy density value (1st cycle) for Li-S coin battery-80:

$820 \times 2.15 \times 6.45/52.71 = 216\ \text{Wh} \cdot \text{kg}_{\text{cell}}^{-1}$

Therefore, for the high loading of the Li-S batteries, the low E/S ratio and thin lithium anode is critical for reducing the total battery weight and consequently achieving a high cell-level gravimetric energy density.

Table S8. Comparison of the areal capacity of Z-PMIA separator at the condition of high sulfur loading with that of other reported electrospun-based separator materials.

Materials	Sulfur loading (mg cm^{-2})	Current density (mA cm^{-2})	Initial areal capacities (mA h cm^{-2})	After areal capacities (mAh cm^{-2})	Reference
PAN@APP	6.0	2.01	3.66	3.29	[17]
BNNs@CNFs-rGO@Ru SAs	5.8	0.69	--	4.4	[16]
MOFs-9.0-NSP	5.12	8.57	5.37	4.14	[18]
MoO_2-CNFs	2.5	0.42	3.4	2.5	[19]
rGO-PVDF/PVDF	1.1	0.37	1.5	0.7	[20]
Ce-MOF-2/CNT	2.5	1.00	2.55	2.09	[21]
Cu_2(CuTCPP)	4.0	1.34	--	4.05	[22]
G@PC/PP	6.0	5.00	6.00	4.75	[23]
P-PMIA@ZIF-8	**6.9**	**2.17**	**6.10**	**5.61**	**This work**

1. L. Zhu, J. Wang, J. Liu, Z. Xu, M. S. Nasir, X. Chen, Z. Wang, S. Sun, Q. Ma, J. Liu, J. Feng, J. Liang and W. Yan, *Sensors and Actuators B: Chemical*, 2022, **354**, 131206.
2. Y. Saito, H. Kataoka, E. Quartarone and P. Mustarelli, *J Phys Chem B*, 2002, **106**, 7200.
3. H. Zhao, W. Kang, N. Deng, M. Liu and B. Cheng, *Chem Eng J*, 2020, **384**.
4. G. Jiang, N. Zheng, X. Chen, G. Ding, Y. Li, F. Sun and Y. Li, *Chem Eng J*, 2019, **373**, 1309-1318.
5. H. Chen, Y. Xiao, C. Chen, J. Yang, C. Gao, Y. Chen, J. Wu, Y. Shen, W. Zhang, S. Li, F. Huo and B. Zheng, *ACS Appl Mater Interfaces*, 2019, **11**, 11459-11465.
6. Y.-E. Miao, G.-N. Zhu, H. Hou, Y.-Y. Xia and T. Liu, *J Power Sources*, 2013, **226**, 82-86.
7. M. Chen, C. Xiao, C. Wang, H. Liu, H. Huang and D. Yan, *Nanoscale*, 2018, **10**, 19835-19845.
8. M. Jian, B. Liu, G. Zhang, R. Liu and X. Zhang, *Colloids and Surfaces A: Physicochemical and Engineering Aspects*, 2015, **465**, 67-76.
9. Z. Zhou, T. Zhao, X. Lu, H. Cao, X. Zha and Z. Zhou, *J Power Sources*, 2018, **396**, 542-550.
10. Y. Li, J. Zhu, P. Zhu, C. Yan, H. Jia, Y. Kiyak, J. Zang, J. He, M. Dirican and X. Zhang, *J Memr Sci*, 2018, **552**, 31-42.
11. Y. Xia, Y. F. Liang, D. Xie, X. L. Wang, S. Z. Zhang, X. H. Xia, C. D. Gu and J. P. Tu, *Chem Eng J*, 2019, **358**, 1047-1053.
12. X. Hao, H. Wenren, X. Wang, X. Xia and J. Tu, *J Colloid Interface Sci*, 2020, **558**, 145-154.
13. C.-L. Song, G.-H. Li, Y. Yang, X.-J. Hong, S. Huang, Q.-F. Zheng, L.-P. Si, M. Zhang and Y.-P. Cai, *Chem Eng J*, 2020, **381**, 122701.
14. Z. Wang, W. Huang, J. Hua, Y. Wang, H. Yi, W. Zhao, Q. Zhao, H. Jia, B. Fei and F. Pan, *Small Methods*, 2020, DOI: 10.1002/smtd.202000082, 2000082.
15. N. Wu, J. Wang, C. Liao, L. Han, L. Song, Y. Hu, X. Mu and Y. Kan, *Journal of Energy Chemistry*, 2022, **64**, 372-384.
16. Y. Li, T. Gao, D. Ni, Y. Zhou, M. Yousaf, Z. Guo, J. Zhou, P. Zhou, Q. Wang and S. Guo, *Adv Mater*, 2022, **34**, e2107638.
17. T. Lei, W. Chen, Y. Hu, W. Lv, X. Lv, Y. Yan, J. Huang, Y. Jiao, J. Chu, C. Yan, C. Wu, Q. Li, W. He and J. Xiong, *Adv Energy Mater*, 2018, **8**, 1802441.

18. Z. Chang, Y. Qiao, J. Wang, H. Deng, P. He and H. Zhou, *Energy Storage Materials*, 2020, **25**, 164-171.
19. R. Zhuang, S. Yao, X. Shen and T. Li, *Int J Energ Res*, 2019, **43**, 1111-1120.
20. P. Zhu, J. Zhu, J. Zang, C. Chen, Y. Lu, M. Jiang, C. Yan, M. Dirican, R. Kalai Selvan and X. Zhang, *J Mater Chem A*, 2017, **5**, 15096-15104.
21. X. J. Hong, C. L. Song, Y. Yang, H. C. Tan, G. H. Li, Y. P. Cai and H. Wang, *ACS nano*, 2019, **13**, 1923-1931.
22. M. Tian, F. Pei, M. Yao, Z. Fu, L. Lin, G. Wu, G. Xu, H. Kitagawa and X. Fang, *Energy Storage Materials*, 2019, **21**, 14-21.
23. F. Pei, L. Lin, A. Fu, S. Mo, D. Ou, X. Fang and N. Zheng, *Joule*, 2018, **2**, 323-336.